Appeared in ACM Computer Graphics Proceedings (SIGGRAPH 94)

Generalization of Lambert's Reflectance Model

Michael Oren and Shree K. Nayar
Department of Computer Science, Columbia University
New York, NY 10027

Abstract

Lambert's model for body reflection is widely used in computer graphics. It is used extensively by rendering techniques such as radiosity and ray tracing. For several real-world objects, however, Lambert's model can prove to be a very inaccurate approximation to the body reflectance. While the brightness of a Lambertian surface is independent of viewing direction, that of a rough surface increases as the viewing direction approaches the light source direction. In this paper, a comprehensive model is developed that predicts body reflectance from rough surfaces. The surface is modeled as a collection of Lambertian facets. It is shown that such a surface is inherently non-Lambertian due to the foreshortening of the surface facets. Further, the model accounts for complex geometric and radiometric phenomena such as masking, shadowing, and interreflections between facets. Several experiments have been conducted on samples of rough diffuse surfaces, such as, plaster, sand, clay, and cloth. All these surfaces demonstrate significant deviation from Lambertian behavior. The reflectance measurements obtained are in strong agreement with the reflectance predicted by the model.

CR Descriptors: I.3.7 [**Computer Graphics**]: Three-Dimensional Graphics and Realism; I.3.3 [**Computer Graphics**]: Picture/Image Generation; J.2 [**Physical Sciences and Engineering**]: Physics.

Additional Key Words: reflection models, Lambert's model, BRDF, rough surfaces, moon reflectance.

1 Introduction

An active area of research in computer graphics involves the creation of realistic images. Images are rendered using one of two well-known techniques, namely, ray tracing [34] or radiosity [6]. The quality of a rendered image depends to a great extent on the accuracy of the reflectance model used. In the past decade, computer graphics has witnessed the application of several physically-based reflectance models for image rendering (see [7], [16], [9], [13]). Reflection from a surface can be broadly classified into two categories: *surface* reflectance which takes place at the interface between two media with different refractive indices and *body* reflectance which is due to *subsurface scattering*. Most of the previous work on physically-based rendering has focused on accurate modeling of surface reflectance. They predict ideal specular reflection from smooth surfaces as well as wide directional lobes from rougher surfaces [13]. In contrast, the body component has most often been assumed to be Lambertian. A Lambertian surface appears equally bright from all directions. This model was advanced by Lambert [18] more than 200 years ago and remains one of the most widely used models in computer graphics.

For several real-world objects, however, the Lambertian model can prove to be a poor and inadequate approximation to body reflection. Figure 1(a) shows a real image of a clay vase obtained using a CCD camera. The vase is illuminated by a single distant light source in the same direction as the sensor. Figure 1(b) shows a rendered image of a vase with the same shape as the one shown in Figure 1(a). This image is rendered using Lambert's model, and the same illumination direction as in the case of the real vase. As expected, Lambert's model predicts that the brightness

(a) (b)

Figure 1: (a) Real image of a cylindrical clay vase. (b) Image of the vase rendered using the Lambertian reflectance model. In both cases, illumination is from the viewing direction.

of the cylindrical vase will decrease as we approach the occluding boundaries on both sides. However, the real vase is very flat in appearance with image brightness remaining almost constant over the entire surface. The vase is clearly *not* Lambertian [1]. This deviation from Lambertian behavior can be significant for a variety of real-world materials, such as, concrete, sand, and cloth. An accurate model that describes body reflection from such commonplace surfaces is imperative for realistic image rendering.

[1]Note that the real vase does not have any significant specular component, in which case, a vertical highlight would have appeared in the middle of the vase.

What makes the vase shown in Figure 1(a) non-Lambertian? We show that the primary cause for this deviation is the roughness of the surface. Figure 2 illustrates the relationship between magnification and reflectance (also see [16]). The reflecting surface may be viewed as a collection of planar facets. At high magnification, each picture element (rendered pixel) includes a single facet. At lower magnifications, each pixel can include a large number of facets. Though the Lambertian assumption is often reasonable when looking at a single planar facet, the reflectance is not Lambertian when a collection of facets is imaged onto a single pixel. This deviation is significant for very rough surfaces, and increases with the angle of incidence. In this paper, we develop a comprehensive model that predicts body reflectance from rough surfaces, and provide experimental results that support the model. Lambert's model is an instance, or limit, of the proposed model.

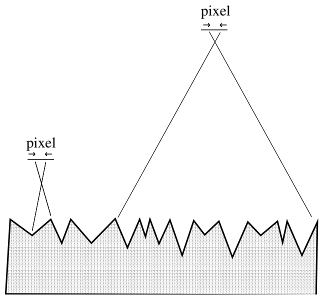

Figure 2: The roughness of a surface causes its reflectance properties to vary with image magnification.

The topic of rough surfaces has been extensively studied in the areas of applied physics, geophysics and engineering. The development of the first few models were primarily motivated to describe the non-Lambertian behavior of the moon. Some of the models are empirical such as Opik's model [22] and its modification by Minnaert [19]. These models do not have any physical foundation and have been found to be incorrect. In contrast, Smith [29] and Buhl *et al.* [3] attempted to develop theoretical models for reflectance from rough surfaces. Smith modeled the rough surface as a random process and assumed each point on the surface to be Lambertian in reflectance. Smith's analysis, however, was confined to the plane of incidence and is not easily extensible to reflections outside this plane. Moreover, Smith's model does not account for interreflection effects. Buhl *et al.* [3] modeled the surface as a collection of spherical cavities. They analyzed interreflections using this surface model, but did not present a complete model that accounts for masking and shadowing effects for arbitrary angles of reflection and incidence. Subsequently, Hering and Smith [14] derived a detailed thermal emission model for surfaces modeled as a collection of V-cavities. However, all cavities are assumed to be identical and aligned in the same direction, namely, perpendicular to the source-viewer plane. Further, the model is limited to the plane of incidence.

More recently, body reflection has emerged as a topic of interest in the graphics community. Poulin and Fournier [26] derived a reflectance function for anisotropic surfaces modeled as a collection of parallel cylindrical sections. Addressing a different cause for non-Lambertian reflectance from the one discussed here, Hanrahan and Krueger [10] used linear transport theory to analyze subsurface scattering from a multi-layered surface. Other researchers in graphics have numerically pre-computed fairly complex reflectance functions and stored the results in the form of look-up tables or coefficients of spherical harmonic expansion (for examples, see [4] [16] [33]). This approach, though practical in many instances, does not replace the need for accurate analytical reflectance models.

The reflectance model developed here can be applied to isotropic as well as anisotropic rough surfaces, and can handle arbitrary source and viewer directions. Further, it takes into account complex geometrical effects such as *masking*, *shadowing*, and *interreflections* between points on the surface. We begin by modeling the surface as a collection of long symmetric V-cavities. Each V-cavity has two opposing facets and each facet is assumed to be much larger than the wavelength of incident light. This surface model was used by Torrance and Sparrow [30] to describe incoherent directional component of surface reflection from rough surfaces. Here, we assume the facets to be Lambertian [2]. First, we develop a reflectance model for anisotropic surfaces with one type (facet-slope) of V-cavities, with all cavities aligned in the same direction on the surface plane. Next, this result is used to develop a model for the more general case of isotropic surfaces that have normal facet distributions with zero mean and arbitrary standard deviation. The standard deviation parameterizes the *macroscopic* roughness of the surface. The fundamental result of our work is that the body reflectance from rough surfaces is not uniform but increases as the viewer moves toward the source direction. This deviation from Lambert's law is not predicted by any previous reflectance model.

We present several experimental results that demonstrate the accuracy of our model. The experiments were conducted on real samples such as sand, plaster, and cloth. In all cases, reflectance predicted by the model was found to be in strong agreement with measurements. The derived model has been implemented as a shading function in RenderMan [32]. We conclude by comparing real and rendered images of a variety of objects. These results demonstrate two points that are fundamental to computer graphics. (a) Several real-world objects have body reflection components that are significantly non-Lambertian. (b) The model presented in this paper can be used to create realistic images of a variety of real-world objects.

2 Surface Roughness Model

The effects of shadowing, masking and interreflection need to be analyzed in order to obtain an accurate reflectance model. To accomplish this, we use the roughness model proposed by Torrance and Sparrow [30] that assumes the surface to be composed of long symmetric V-cavities (see Figure 3). Each cavity consists of two planar facets. The width of each facet is assumed to be small compared to its length. We assume each facet area da is small compared to the area dA of the surface patch that is imaged by a single sensor pixel. Hence, each pixel includes a very large number of facets. Further, the facet area is large compared to the wavelength λ of incident light, and therefore geometrical optics can be used to derive the reflectance model. The above assumptions can be summarized as: $\lambda^2 \ll da \ll dA$

We denote the slope and orientation of each facet in the V-cavity model as (θ_a, ϕ_a), where θ_a is the polar angle and

[2]This assumption does not limit the implications of the reflectance model presented here. The non-Lambertian behavior reported here is expected for a wide range of local body reflectance models (see [5], for example) since surface roughness is shown to play a dominant role.

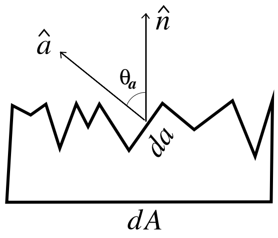

Figure 3: Surface modeled as a collection of V-cavities.

ϕ_a is the azimuth angle. Torrance and Sparrow have assumed all facets to have equal area da. They use the distribution $N(\theta_a, \phi_a)$ to represent the number of facets per unit surface area that have the normal $\hat{a} = (\theta_a, \phi_a)$. Here, we use a probability distribution to represent the fraction of the surface area that is occupied by facets with a given normal. This is referred to as the *slope-area distribution* $P(\theta_a, \phi_a)$. The facet-number distribution and the slope-area distribution are related as follows:

$$P(\theta_a, \phi_a) = N(\theta_a, \phi_a)\, da \, \cos\theta_a \tag{1}$$

The slope-area distribution is easier to use than the facet-number distribution in the following model derivation. For isotropic surfaces, $N(\theta_a, \phi_a) = N(\theta_a)$ and $P(\theta_a, \phi_a) = P(\theta_a)$, since the distributions are rotationally symmetric with respect to the global surface normal $\hat{n}$ (Figure 3).

3 Reflectance Model

In this section, we derive a reflectance model for rough diffuse surfaces. For lack of space, only important results are discussed. For details we refer the reader to Oren and Nayar [23, 24]. During the derivation, we will draw on several well-known radiometric definitions that are given in [20].

Consider a surface area dA that is imaged by a single sensor element in the direction $\hat{v} = (\theta_r, \phi_r)$ and illuminated by a distant point light source in the direction $\hat{s} = (\theta_i, \phi_i)$. The area dA is composed of a very large number of symmetric V-cavities. Each V-cavity is composed of two facets with the same slope but facing in opposite directions. Consider the flux reflected by a facet with area da and normal $\hat{a} = (\theta_a, \phi_a)$. The projected area on the surface occupied by the facet is $da \cos\theta_a$ (see Figure 3). Thus, while computing the contribution of the facet to the radiance of the surface patch, we need to use the projected area $da \cos\theta_a$ and not the actual facet area da. This radiance contribution is what we call the *projected radiance* of the facet:

$$L_{rp}(\theta_a, \phi_a) = \frac{d\Phi_r(\theta_a, \phi_a)}{(da \cos\theta_a)\, \cos\theta_r \, d\omega_r} \tag{2}$$

where, $d\omega_r$ is the solid angle subtended by the sensor optics. For ease of description, we have dropped the source and viewing directions from the notations for projected radiance and flux. Now consider the slope-area distribution of facets given by $P(\theta_a, \phi_a)$. The total radiance of the surface can be obtained as the aggregate of $L_{rp}(\theta_a, \phi_a)$ over all facets on the surface:

$$L_r(\theta_r, \phi_r; \theta_i, \phi_i) = \int_{\theta_a=0}^{\frac{\pi}{2}} \int_{\phi_a=0}^{2\pi} P(\theta_a, \phi_a)\, L_{rp}(\theta_a, \phi_a)\, \sin\theta_a \, d\phi_a \, d\theta_a \tag{3}$$

3.1 Model for Uni-directional Single-Slope Distribution

The first surface type we consider has all facets with the same slope θ_a. Further, all V-cavities are aligned in the same direction; azimuth angles of all facets are either ϕ_a or $\phi_a + \pi$. Consider a Lambertian facet with albedo ρ, that is fully illuminated (no shadowing) and is completely visible (no masking) from the sensor direction. The radiance of the facet is proportional to its irradiance and is equal to $\frac{\rho}{\pi} E(\theta_a, \phi_a)$. The irradiance of the facet is $E(\theta_a, \phi_a) = E_0 \langle \hat{s}, \hat{a} \rangle$, where, E_0 is the irradiance when the facet is illuminated head-on (i.e. $\hat{s} = \hat{n}$), and $\langle \, , \, \rangle$ denotes the dot product between two vectors. Using the definition of radiance [20], the flux reflected by the facet in the sensor direction is: $d\Phi_r = \frac{\rho}{\pi} E_0 \langle \hat{s}, \hat{a} \rangle \langle \hat{v}, \hat{a} \rangle$. Substituting this expression in (2), we get:

$$L_{rp}(\theta_a, \phi_a) = \frac{\rho}{\pi} E_0 \frac{\langle \hat{s}, \hat{a} \rangle \langle \hat{v}, \hat{a} \rangle}{\langle \hat{a}, \hat{n} \rangle \langle \hat{v}, \hat{n} \rangle} \tag{4}$$

The above expression clearly illustrates that the projected radiance of a tilted Lambertian facet is not equal in all viewing directions.

Geometric Attenuation Factor: If the surface is illuminated and viewed from the normal direction ($\hat{s} = \hat{v} = \hat{n}$), all facets are fully illuminated and visible. For larger angles of incidence and reflection, however, facets are shadowed and masked by adjacent facets (see Figure 4). Both these geometrical phenomena reduce the projected radiance of the facet. This reduction in brightness can be derived using geometry and incorporated into a single term, called the *geometrical attenuation factor* ($\mathcal{GAF}$), that lies between zero and unity. Several derivations of the $\mathcal{GAF}$ have been presented [30] [2] [23]. The final result can be compactly represented as:

$$\mathcal{GAF} = Min\left[1, Max\left[0, \frac{2\langle \hat{s}, \hat{n} \rangle \langle \hat{a}, \hat{n} \rangle}{\langle \hat{s}, \hat{a} \rangle}, \frac{2\langle \hat{v}, \hat{n} \rangle \langle \hat{a}, \hat{n} \rangle}{\langle \hat{v}, \hat{a} \rangle}\right]\right] \tag{5}$$

The above $\mathcal{GAF}$ is valid for any facet normal, $\hat{a}$, not necessarily the bisector of the angle between the source and the sensor direction.

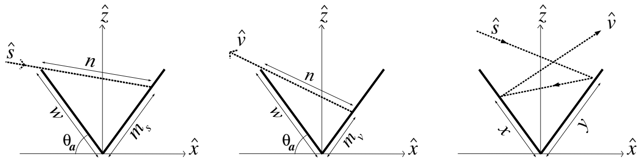

(a) Shadowing (b) Masking (c) Interreflection

Figure 4: Shadowing, masking and interreflection in a V-cavity

Projected Radiance and $\mathcal{GAF}$: The projected radiance of a Lambertian facet is obtained by multiplying the projected radiance given by (4) with the $\mathcal{GAF}$ given by (5).

$$L^1_{rp}(\theta_a, \phi_a) = \frac{\rho}{\pi} E_0 \frac{\langle \hat{s}, \hat{a} \rangle \langle \hat{v}, \hat{a} \rangle}{\langle \hat{a}, \hat{n} \rangle \langle \hat{v}, \hat{n} \rangle} \mathcal{GAF}(\hat{s}, \hat{v}, \hat{a}) \tag{6}$$

Note that the projected radiance is denoted as L^1_{rp}; the superscript is used to indicate that the radiance is due to direct illumination by the source. In the following discussion, we will use L^2_{rp} to denote radiance due to interreflections.

Interreflection Factor: We have the task of modeling interreflections in the presence of masking and shadowing effects. In the case of Lambertian surfaces, the energy in an incident light ray diminishes rapidly with each interreflection bounce. Therefore, we model only two-bounce interreflections and ignore subsequent bounces. Since the length l of the V-cavity is much larger than its width w, i.e. $l \gg w$, it can be viewed as a one-dimensional shape with translational symmetry. For such shapes, the two-bounce interreflection component can be determined as an integral over the one-dimensional cross-section of the shape [28]:

$$L_r^2(x) = \frac{\rho}{\pi} \int K'(x,y) L_r^1(y) dy \qquad (7)$$

where x and y are the shortest distances of facet points from the intersection of the two facets (see Figure 4(c)). K' is the kernel for the translational symmetry case and is derived in [15] and [8] to be:

$$K'(x,y) = \frac{\pi \sin^2(2\theta_a)}{2} \frac{xy}{(x^2 + 2xy\cos(2\theta_a) + y^2)^{3/2}} \qquad (8)$$

We know that the orientation of the considered facet is $\hat{a} = (\theta_a, \phi_a)$ and the orientation of the adjacent facet is $\hat{a}' = (\theta_a, \phi_a + \pi)$. The limits of the integral in the interreflection equation are determined by the masking and shadowing of these two facets. Let m_v be the width of the facet which is visible to the viewer, and m^s be the width of the *adjacent* facet that is illuminated. From the definitions of radiance and projected radiance we get:

$$L_{rp}^2 = \frac{l < \hat{a}, \hat{v} >}{da < \hat{a}, \hat{n} > < \hat{v}, \hat{n} >} \int_{x=m_v}^{w} L_r^2(x)\, dx \qquad (9)$$

Using the following change of variables: $t = \frac{x}{w}$; $r = \frac{y}{w}$, the radiance due to two-bounce interreflections given by (7) and (9) can be written as:

$$L_{rp}^2 = (\frac{\rho}{\pi})^2 E_0 \frac{< \hat{a}', \hat{s} > < \hat{a}, \hat{v} >}{< \hat{a}, \hat{n} > < \hat{v}, \hat{n} >} \int_{t=\frac{m_v}{w}}^{1} \int_{r=\frac{m^s}{w}}^{1} K'(t,r) dr\, dt \qquad (10)$$

Using (8), the above integral is evaluated as:

$$\int_{t=\frac{m_v}{w}}^{1} \int_{r=\frac{m^s}{w}}^{1} K'(r,t) dr\, dt = \qquad (11)$$

$$\frac{\pi}{2} \left[d(1, \frac{m_v}{w}) + d(1, \frac{m^s}{w}) - d(\frac{m^s}{w}, \frac{m_v}{w}) - d(1,1) \right]$$

where: $d(x,y) = \sqrt{x^2 + 2xy\cos(2\theta_a) + y^2}$. We refer to right hand side of equation (11) as the *interreflection factor* ($\mathcal{IF}$). The total projected radiance of the facet is the sum of two the components, the radiance due to direct source illumination given by equation (6) and the above interreflection component. Therefore, $L_{rp}(\theta_a, \phi_a) = L_{rp}^1(\theta_a, \phi_a) + L_{rp}^2(\theta_a, \phi_a)$. The uni-directional single-slope surface considered here has only two types of facets with normals (θ_a, ϕ_a) and $(\theta_a, \phi_a + \pi)$. Hence, the radiance of the surface for any given source and sensor directions is simply the average of the projected radiances of the two facet types.

3.2 Model for Isotropic Single-Slope Distribution

All facets on this isotropic surface have the same slope θ_a but are uniformly distributed in ϕ_a. As we did in the previous section, we evaluate the projected radiance as the sum of two components: projected radiance due to direct illumination, $L_{rp}^1(\theta_a)$, and projected radiance due to interreflection, $L_{rp}^2(\theta_a)$. In the previous section, we calculated each of the two components for a single facet with normal $\hat{a} = (\theta_a, \phi_a)$. Therefore, the radiance of the isotropic surface is determined as an integral of the projected radiance over ϕ_a:

$$L_{rp}^i(\theta_a) = \frac{1}{2\pi} \int_{\phi_a=0}^{2\pi} L_{rp}^i(\theta_a, \phi_a) d\phi_a \qquad (i = 1,2) \quad (12)$$

Given a source direction (θ_i, ϕ_i) and a sensor direction (θ_r, ϕ_r), we first find the ranges of facet orientation ϕ_a for which the facets are masked, shadowed, masked and shadowed, and neither masked nor shadowed[3]. This requires careful geometrical analysis. Then the above integral is decomposed into parts corresponding to masking/shadowing ranges. Each range is evaluated using the corresponding radiance expressions (6) and (11).We refer the interested reader to Oren and Nayar [23, 24] for details.

3.3 Model for Gaussian Slope-Area Distribution

The surface considered above consists of V-cavities with a single facet slope. Realistic surfaces can be modeled only if the slope-area distribution $P(\theta_a, \phi_a)$ includes a variety of different facet slopes. If the surface roughness is isotropic, the slope-area distribution can be described using a single parameter namely θ_a since the facets are uniformly distributed in ϕ_a. The two components of the radiance of any isotropic surface can therefore be determined as:

$$L_r^i(\theta_r, \theta_i, \phi_r - \phi_i) = \int_0^{\frac{\pi}{2}} P(\theta_a) L_{rp}^i(\theta_a) \sin\theta_a\, d\theta_a \qquad (13)$$
$$(i = 1,2)$$

where $L_{rp}^i(\theta_a)$ $(i = 1,2)$ are the projected radiance components obtained in the previous section. Here, we assume the isotropic distribution to be Gaussian with mean μ and standard deviation σ, i.e. $P(\theta_a; \sigma, \mu)$. Reasonably rough surfaces can be described using a zero mean ($\mu = 0$) Gaussian distribution: $P(\theta_a) = c\, exp\left(-\theta_a^2/2\sigma^2\right)$ where c is the normalization constant.

3.4 Functional Approximation

The reflectance model is to be obtained by evaluating integral (13) using the results of section 3.2 and the Gaussian distribution, $P(\theta_a; \sigma, 0)$. The resulting integral cannot be easily evaluated. Therefore, we pursued a functional approximation to the integral that is accurate for arbitrary surface roughness and angles of incidence and reflection. In deriving this approximation, we carefully studied the functional forms of $L_{rp}^i(\theta_a)$ $(i = 1,2)$ which were evaluated in the previous step (the details can be found in Oren and Nayar [23, 24]). This enabled us to identify basis functions that can be used in the approximation. Then, we conducted a large set of numerical evaluations of the integral in (13) by varying surface roughness σ, the angles of incidence (θ_i, ϕ_i) and reflection (θ_r, ϕ_r). These evaluations and the identified basis functions were used to arrive at an accurate functional approximation for surface radiance. This procedure was applied independently to the source illumination component as well as the interreflection component.

The final approximation results are given below. We define $\alpha = Max[\theta_r, \theta_i]$ and $\beta = Min[\theta_r, \theta_i]$. The source illumination component of radiance of a surface with roughness σ is:

[3] Imagine a V-cavity rotated about the global surface normal for any given source and sensor direction. Various masking/shadowing scenarios can be visualized.

$$L_r^1(\theta_r,\theta_i,\phi_r-\phi_i;\sigma) = \frac{\rho}{\pi}E_0\cos\theta_i\Bigg[C_1(\sigma)+ \cos(\phi_r-\phi_i)C_2(\alpha;\beta;\phi_r-\phi_i;\sigma)\tan\beta + \big(1-|\cos(\phi_r-\phi_i)|\big)C_3(\alpha;\beta;\sigma)\tan\left(\frac{\alpha+\beta}{2}\right)\Bigg] \tag{14}$$

where the coefficients are:

$$C_1 = 1-0.5\frac{\sigma^2}{\sigma^2+0.33}$$

$$C_2 = \begin{cases} 0.45\frac{\sigma^2}{\sigma^2+0.09}\sin\alpha & \text{if } \cos(\phi_r-\phi_i)\geq 0 \\ 0.45\frac{\sigma^2}{\sigma^2+0.09}\left(\sin\alpha-(\frac{2\beta}{\pi})^3\right) & \text{otherwise} \end{cases}$$

$$C_3 = 0.125\left(\frac{\sigma^2}{\sigma^2+0.09}\right)\left(\frac{4\alpha\beta}{\pi^2}\right)^2$$

The approximation to the interreflection component is:

$$L_r^2(\theta_r,\theta_i,\phi_r-\phi_i;\sigma) = 0.17\frac{\rho^2}{\pi}E_0\cos\theta_i\,\frac{\sigma^2}{\sigma^2+0.13}\left[1-\cos(\phi_r-\phi_i)\left(\frac{2\beta}{\pi}\right)^2\right] \tag{15}$$

The two components are combined to obtain the total surface radiance:

$$L_r(\theta_r,\theta_i,\phi_r-\phi_i;\sigma) = L_r^1(\theta_r,\theta_i,\phi_r-\phi_i;\sigma) + L_r^2(\theta_r,\theta_i,\phi_r-\phi_i;\sigma) \tag{16}$$

Finally, the *BRDF* of the surface is obtained from its radiance and irradiance as $f_r(\theta_r,\theta_i,\phi_r-\phi_i;\sigma) = L_r(\theta_r,\theta_i,\phi_r-\phi_i;\sigma)\,/\,E_0\cos\theta_i$. It is important to note that the approximation presented above obeys Helmholtz's reciprocity principle (see [1]). *Also note that the above model reduces to the Lambertian model when $\sigma=0$.* Note that by substituting the albedo as function of the wavelength, $\rho(\lambda)$, the dependency of the model on the wavelength comes out explicitly.

In the next section, we present several experimental results that verify the above diffuse reflectance model. Here, we give a brief illustration of the main characteristics of the model. Figure 5 shows the reflectance predicted by the model for a very rough surface with $\sigma=30°$ and $\rho=0.9$. The radiance L_r in the plane of incidence ($\phi_r=\phi_i,\phi_i+\pi$) is plotted as a function of the reflection angle θ_r for incidence angle $\theta_i=75°$. Two curves are shown in the figure, both obtained by the numerical evaluation of the integral in (13).

The first curve (solid line) includes both direct illumination and interreflection components of radiance, while the second (thin line) is only the direct illumination component. Notice that these radiance plots deviate substantially from Lambertian reflectance. *Surface radiance increases as the viewing direction approaches the source direction.* The curves can be divided into three sections. In the *backward* (source) direction, the radiance is maximum and gets "cut-off" due to strong masking effects when θ_r exceeds θ_i. This cut-off occurs exactly at $\theta_r=\theta_i$ and is independent of roughness. In the middle section of the plot, radiance varies approximately as a scaled $tan\,\theta_r$ function with constant offset. Finally, interreflections dominate in the *forward* direction where most facets are self-shadowed and the visible facets receive light primarily from adjacent facets. This is illustrated by the difference between the two curves.

In Figure 6(a), the effect of varying the incidence angle θ_i is shown. Here we have chosen to plot *BRDF* rather than radiance to better illustrate the effect of varying θ_i. It is

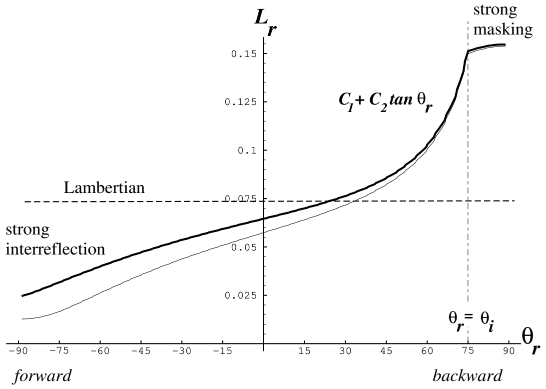

Figure 5: Diffuse reflectance in the plane of incidence for a surface with $\sigma=30°$, $\rho=0.90$, and incidence angle $\theta_i=75°$. The thin line is radiance due to direct illumination (without interreflections).

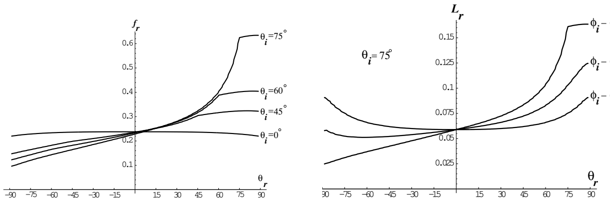

(a) (b)

Figure 6: (a) *BRDF* for different angles of incidence. (b) Radiance outside the plane of incidence. In both plots, $\sigma=40°$ and $\rho=0.9$.

interesting to note that the model predicts near-Lambertian behavior for very small incidence angles ($\theta_i\approx 0$). This results from both facets of a V-cavity having nearly equal irradiance for small angles of incidence. As the incidence angle increases, the backscatter phenomenon begins to dominate. Figure 6(b) shows the effect of placing the sensor outside the plane of incidence. When the sensor-normal plane is perpendicular to the source-normal plane, the rough surface again exhibits near-Lambertian characteristics.

3.5 Qualitative Model

In this section, we propose a further simplification to the reflectance model presented in the previous section. In order to obtain this simplification, a slight sacrifice in accuracy must be made. In return, some computations can be saved during image rendering. The following simplified model was arrived at by studying, through numerous simulations, the relative significance of various terms in the functional approximation given by (14). The simulations showed that coefficient C_3 makes a relatively small contribution to the total radiance. A simpler model is thus obtained by discarding C_3 and ignoring interreflections:

$$L_r(\theta_r,\theta_i,\phi_r-\phi_i;\sigma) = \frac{\rho}{\pi}E_0\cos\theta_i(A+B\,Max\Big[0,\cos(\phi_r-\phi_i)\Big]\sin\alpha\tan\beta) \tag{17}$$

$$A = 1.0-0.5\frac{\sigma^2}{\sigma^2+0.33}$$

$$B = 0.45\frac{\sigma^2}{\sigma^2+0.09}$$

The two coefficients A and B are obtained directly from C_1 and C_2, respectively. Note that the qualitative model also reduces to the Lambertian model when $\sigma = 0$.

4 Experimental Verification

We have conducted several experiments to verify the accuracy of the reflectance model. The experimental set-up ([23, 24]) used to measure the radiance of samples is shown in figure 7.

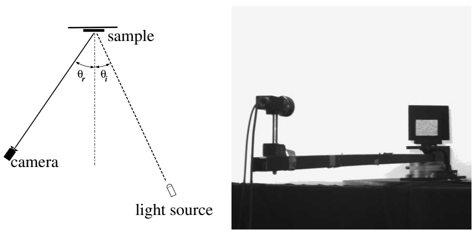

Figure 7: Sketch and photograph of the set-up used to measure reflectance.

Figures 8 and 9 shows results obtained for samples of wall plaster (A) and sand (B). The radiance of each sample is plotted as a function of sensor direction θ_r for different angles of incidence θ_i. These measurements are made in the plane of incidence ($\phi_r = \phi_i = 0$). The measured brightness values, shown as dots, are compared with those predicted by the model plotted as solid lines. For these two samples (A and B), σ and ρ were selected empirically to obtain the best match between measured and predicted reflectance. Here, we have used the numerical evaluation of the model (equation 13). For both samples, radiance increases as the viewing direction θ_r approaches the source direction θ_i (backward reflection). This is in contrast to the behavior of rough specular surfaces that reflect more in the forward direction, or Lambertian surfaces where radiance does not vary with viewing direction. For both samples, the model predictions and experimental measurements match remarkably well. In both cases, a small peak is noticed near the source direction. This phenomenon is known as the *opposition effect* or retroreflection. It is a sharp peak close to the source direction and is caused by a different backscattering mechanism from the one described by our model. (see [12, 17, 31, 21, 27, 11]).

Figures 10 and 11 show results for a sample C (foam) and sample D (cloth) that has not only a body reflectance component but also a significant surface reflection component. In this case, the reflectance model used is a linear combination of new model and the Torrance-Sparrow model [30] that describes the incoherent directional component of surface reflection and which is based on the same surface model (long symmetric V-cavities): $L_r = k_b L_r^b + k_s L_r^s$, where L_r^b and L_r^s are the body and surface reflection components, respectively. k_b and k_s are weighting coefficients for the two components. For this experiment, we used the functional approximation and the reflectance parameters σ, ρ, k_b, and k_s were estimated by fitting (using non-linear optimization) the model to measured data. Additional experiments are reported in Oren and Nayar [23].

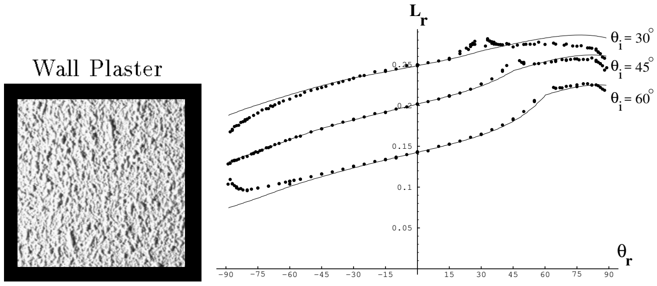

Figure 8: Reflectance measurement and reflectance model (using $\sigma = 30°$, $\rho = 0.90$) plots for wall plaster (sample A). Radiance is plotted as a function of sensor direction (θ_r) for different angles of incidence ($\theta_i = 30°, 45°, 60°$).

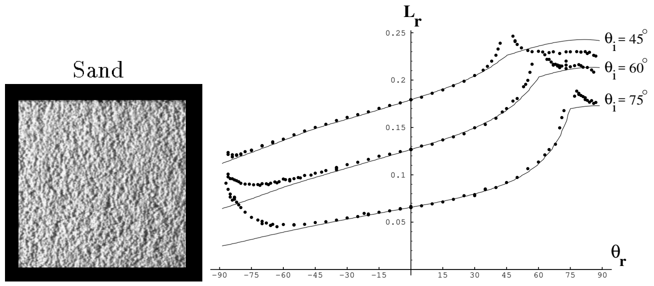

Figure 9: Reflectance measurement and reflectance model (using $\sigma = 35°$, $\rho = 0.80$) plots for white sand (sample B).

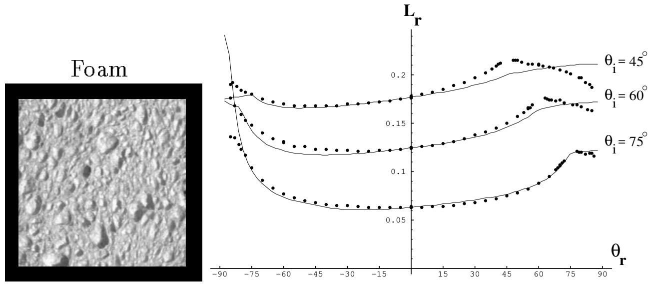

Figure 10: Reflectance measurement and reflectance model ($\sigma = 20°$, $\rho = 0.8$, $k_s/k_b = 0.019$) plots for foam (sample C).

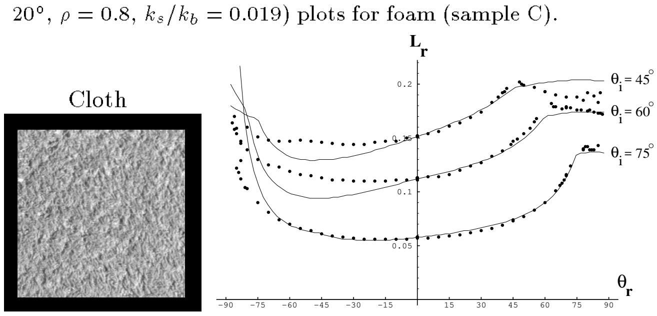

Figure 11: Reflectance measurement and reflectance model ($\sigma = 42°$, $\rho = 0.75$, $k_s/k_b = 0.085$) plots for a cotton towel (sample D).

5 Implications for Graphics

In this section, we describe the implications of the proposed model for realistic rendering. Figure 12(a) shows a real image of the rough cylindrical clay vase discussed in the introduction. Figure 12(b) shows a rendered image of the vase using the Lambertian model and its known geometry. Clearly, this rendered image does not match the real image of the vase. On the other hand, the appearance of the rendered vase using the proposed reflectance model, shown in Figure 12(c), closely resembles the real vase. The model parameters $\rho = 0.7$ and $\sigma = 40°$ were chosen empirically to obtain the best fit to the measured brightness values. Figure 13(a) compares brightness values along the cross-section of the three different vase images in Figure 12. It is interesting to note that the brightness of the real vase remains nearly constant over most of the cross-section and drops quickly to zero very close to the limbs. The proposed model does very well in predicting this behavior, while the Lambertian model produces large brightness errors. Figure 13(b) shows similar plots for illumination from $20°$ to the right of the sensor. In this case, brightness variation on the real vase is asymmetric. Once again, the proposed model closely matches the real image. However, the Lambertian model forces the brightness close to the right limb of the vase to drop much faster than in the real image. As a result, the brightness peak predicted by the Lambertian model is significantly away from the actual peak.

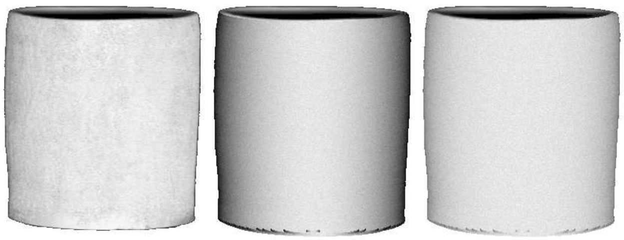

(a) Image (b) Lambertian (c) Model

Figure 12: Real image of a cylindrical clay vase compared with images rendered using the Lambertian and proposed models. Illumination is from the camera direction.

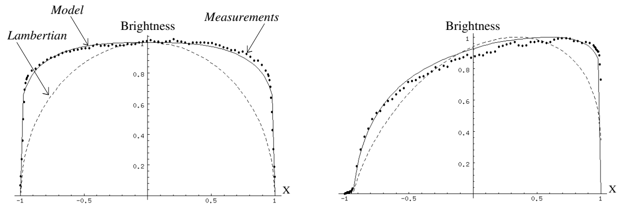

(a) (b)

Figure 13: Comparison between image brightness along the cross-section of the real vase, and vases rendered using the Lambertian and proposed models. (a) $\theta_i = 0°$. (b) $\theta_i = 20°$.

The functional approximation, given by equation (14), and the qualitative model, given by (17), are easily used for realistic rendering. We have implemented the functional approximation as a "shader" using the RenderMan shading language [32]. Figure 14 shows spheres rendered using the shader. In all four cases, the sphere is illuminated from the viewer direction. In the first case, $\sigma = 0$, and hence the sphere appears Lambertian. As the roughness increases, the sphere begins to appear flatter. In the extreme roughness case shown in Figure 14(d), the sphere appears like a flat disc with near constant brightness. This phenomenon has been widely observed and reported in the case of the full moon ([25],[28]).

Finally, Figure 15 shows rendered images of a scene with three matte objects, a vase, cylindrical block and a cube. In Figure 15(a), all three objects have zero macroscopic roughness, i.e. they are Lambertian. Illumination in this case is from the viewer direction. Note that the vase and the cylinder have strong brightness variations, and the three visible faces of the cube have distinctly different brightness values. In Figure 15(b), the scene is again illuminated from the viewer direction, but the three objects have roughness $\sigma = 30°$. Consequently, the shading over the vase and the cylinder is diminished considerably. Furthermore, the contrast between the flat and curved sections of the cylindrical block and also the contrast between the three faces of the cube are reduced substantially. It is important to note that the moderate shading is achieved without any ambient component in the illumination, but rather from modeling of roughness effects.

6 Summary

In conclusion, we have developed a comprehensive model for body reflectance from surfaces with macroscopic roughness. A model was first derived for anisotropic surfaces that have facets with only one slope. This result was used to develop a model for isotropic surfaces with Gaussian slope-area distribution. We have also presented a qualitative model for diffuse reflection that has a simple functional form. Numerous experiments were conducted to verify the reflectance mechanism described in this paper. Real and rendered images of diffuse objects were compared to demonstrate that the proposed model has important implications for computer graphics.

REFERENCES

[1] P. Beckmann and A. Spizzichino. *The Scattering of Electromagnetic Waves from Rough Surfaces.* Pergamon, New York, 1963.

[2] J. F. Blinn. Models of light reflection for computer synthesized pictures. *ACM Computer Graphics (SIGGRAPH 77)*, 19(10):542–547, 1977.

[3] D. Buhl, W. J. Welch, and D. G. Rea. Reradiation and thermal emission from illuminated craters on the lunar surface. *Journal of Geophysical Research*, 73(16):5281–5295, August 1968.

[4] B. Cabral, N. Max, and R. Springmeyer. Bidirectional reflection functions from surface bump maps. *ACM Computer Graphics (SIGGRAPH 87)*, 21(4):273–281, 1987.

[5] S. Chandrasekhar. *Radiative Transfer.* Dover Publications, 1960.

[6] M. F. Cohen and D. P. Greenberg. The hemi-cube, a radiosity solution for complex environments. *ACM Computer Graphics (SIGGRAPH 85)*, 19(3):31–40, 1985.

[7] R. L. Cook and K. E. Torrance. A reflection model for computer graphics. *ACM Transactions on Graphics*, 1(1):7–24, 1982.

[8] D. Forsyth and A. Zisserman. Mutual illumination. *Proc. Conf. Computer Vision and Pattern Recognition*, pages 466–473, 1989.

[9] R. Hall. *Illumination and Color in Computer Generated Imagery.* Springer-Verlag, 1989.

[10] P. Hanrahan and W. Krueger. Reflection from layered surfaces due to subsurface scattering. *Computer Graphics Proceedings (SIGGRAPH 93)*, pages 165–174, 1993.

[11] B. W. Hapke, R. M. Nelson, and W. D. Smythe. The opposition effect of the moon: The contribution of coherent backscatter. *Science*, 260(23):509–511, April 1993.

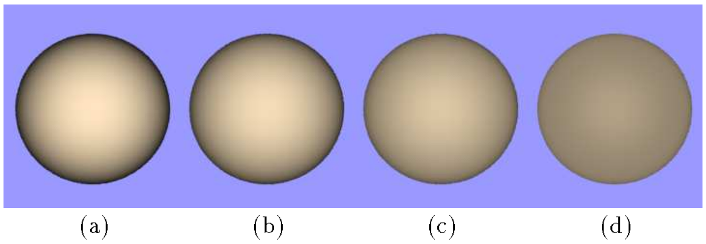

Figure 14: Images of spheres rendered using the proposed reflectance model: (a) $\sigma = 0$ (Lambertian sphere); (b) $\sigma = 10°$; (c) $\sigma = 20°$; and (d) $\sigma = 40°$.

[12] B. W. Hapke and Huge van Horn. Photometric studies of complex surfaces, with applications to the moon. *Journal of Geophysical Research*, 68(15):4545–4570, August 1963.

[13] X. D. He, K. E. Torrance, F. X. Sillion, and D. P. Greenberg. A comprehensive physical model for light reflection. *ACM Computer Graphics (SIGGRAPH 91)*, 25(4):175–186, 1991.

[14] R. G. Hering and T. F. Smith. Apparent radiation properties of a rough surface. *AIAA Progress in Astronautics and Aeronautics*, 23:337–361, 1970.

[15] M. Jakob. *Heat Transfer*. Wiley, 1957.

[16] J. T. Kajiya. Anisotropic reflection model. *ACM Computer Graphics (SIGGRAPH 91)*, 25(4):175–186, 1991.

[17] Y. Kuga and A. Ishimaru. Retroreflectance from a dense distribution of spherical particles. *Journal of the Optical Society of America A*, 1(8):831–835, August 1984.

[18] J. H. Lambert. Photometria sive de mensure de gratibus luminis, colorum umbrae. *Eberhard Klett*, 1760.

[19] M. Minnaert. The reciprocity principle in lunar photometry. *Astrophysical Journal*, 93:403–410, 1941.

[20] F. E. Nicodemus, J. C. Richmond, and J. J. Hsia. *Geometrical Considerations and Nomenclature for Reflectance.* National Bureau of Standards, October 1977. Monograph No. 160.

[21] P. Oetking. Photometric studies of diffusely reflecting surfaces with application to the brightness of the moon. *Journal of Geophysical Research*, 71(10):2505–2513, May 1966.

[22] E. Opik. Photometric measures of the moon and the moon the earth-shine. *Publications de L'Observatorie Astronomical de L'Universite de Tartu*, 26(1):1–68, 1924.

[23] M. Oren and S. K. Nayar. Generalization of the lambertian model and implications for machine vision. Technical Report CUCS-057-92, Department of Computer Science, Columbia University, New York, NY, USA, 1992.

[24] M. Oren and S. K. Nayar. Generalization of lambert's reflectance model. *Proceedings of SIGGRAPH 94*, 1994. CD-ROM version.

[25] N. S. Orlova. Photometric relief of the lunar surface. *Astron. Z*, 33(1):93–100, 1956.

[26] P. Poulin and A. Fournier. A model for anisotropic reflection. *ACM Computer Graphics (SIGGRAPH 90)*, 24(4):273–282, 1990.

[27] T. Shibata, W. Frei, and M. Sutton. Digital correction of solar illumination and viewing angle artifacts in remotely sensed images. *Machine Processing of Remotely Sensed Data Symposium*, pages 169–177, 1981.

[28] R. Siegel and J. R. Howell. *Thermal Radiation Heat Transfer*. Hemisphere Publishing Corporation, third edition, 1972.

[29] B. G. Smith. Lunar surface roughness: Shadowing and thermal emission. *Journal of Geophysical Research*, 72(16):4059–4067, August 1967.

[30] K. Torrance and E. Sparrow. Theory for off-specular reflection from rough surfaces. *Journal of the Optical Society of America*, 57:1105–1114, September 1967.

[31] L. Tsang and A. Ishimaru. Backscattering enhancement of random discrete scatterers. *Journal of the Optical Society of America A*, 1(8):836–839, August 1984.

[32] S. Upstill. *The RenderMan Companion*. Addison Wesley, 1989.

[33] H.W. Westin, J.R. Arvo, and K.E. Torrance. Predicting reflectance functions from complex surfaces. *ACM Computer Graphics (SIGGRAPH 92)*, 26(2):255–264, 1992.

[34] T. Whitted. An improved illumination model for shaded display. *Communications of the ACM*, 23(6):343–349, 1980.

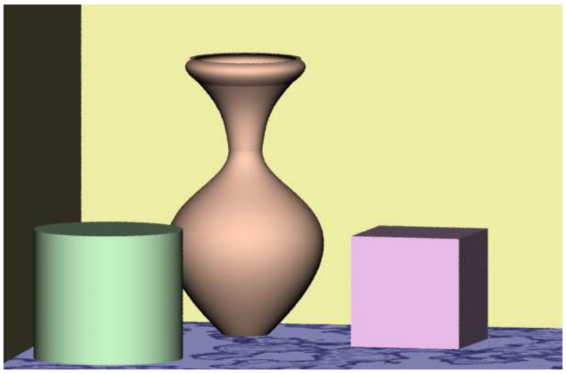

(a)

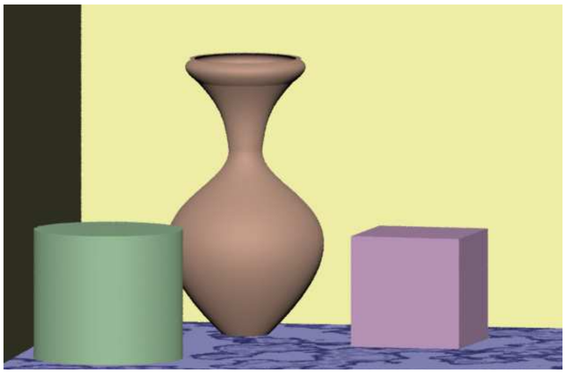

(b)

Figure 15: Scene rendered using the proposed model. All three objects have equal roughness. (a) $\sigma = 0°$; (b) $\sigma = 30°$. The illumination is from the viewing direction.